EFFECT OF TANTALUM CONTENT ON THE MICROSTRUCTURE AND MECHANICAL BEHAVIOR OF CERMETS BASED ON $(Ti_xTa_{1-x})(C_{0.5}N_{0.5})$ SOLID SOLUTIONS

E. Chicardi*[1], Y. Torres[2], J.M. Córdoba[1], P. Hvizdoš[3] and F.J. Gotor[1]

[1]Instituto de Ciencia de Materiales de Sevilla (US-CSIC), Av. Américo Vespucio, 49, 41092 (Sevilla) Spain.

[2]Dpto. de Ingeniería Mecánica y de los Materiales, E.T.S. de Ingeniería, Universidad de Sevilla, Avda. Camino de los Descubrimientos, s/n, 41092 Sevilla, Spain.

[3]Institute of Materials Research, Slovak Academy of Sciences, Košice, Slovakia.

ABSTRACT

Titanium-tantalum carbonitride, (Ti,Ta)(C,N), based cermets with different Ti and Ta contents were prepared using a mechanically induced self-sustaining reaction and then densified using a pressureless sintering process. Complete microstructural and mechanical characterizations were performed on the materials, which revealed that the size of the carbonitride ceramic particle was significantly reduced when the Ta content was increased. The flexural strength and fracture toughness were measured using the ball on three balls test and the indentation microfracture test, respectively. The strength profile was analyzed under the framework of Weibull theory. The change in the mechanical properties as a function of the Ta content was correlated with the normalized microstructural parameters, such as the binder mean free path. The decrease in toughness and flexural strength was attributed to the presence of intermetallic compounds in the binder phase, which was also corroborated by the nanoindentation tests.

Keywords: A. Ceramic-matrix composites; B. Mechanical properties; C. Mechanical testing; D.Powder processing.

*Corresponding Author e-mail: ernesto.chicardi@icmse.csic.es Phone: +34 954 489217 Fax: +34 954 460665

1. INTRODUCTION.

Titanium carbonitride, Ti(C,N), is a solid solution in the TiC-TiN system that exhibits excellent properties, including a high melting point, high hardness, high thermal and electrical conductivities and good thermal and chemical stabilities [1-4]. When Ti(C,N) is combined with a metal binding phase composed of Ni or Co, the resulting cermet material exhibits improved properties, especially with respect to toughness [5]. Ti(C,N)-based cermets also have good wear resistance and have been successfully used as cutting tools when an improved surface finish is required [6]. Furthermore, the combination of low density, high thermal conductivity and good oxidation resistance compared with conventional hard metals makes cermets good candidates for high speed machining applications [4, 7].

Several binary carbides, such as NbC, TaC, Mo_2C or WC, are usually added to Ti(C,N)-based cermets to further improve their properties. Specifically, TaC is introduced to enhance stability at elevated temperatures, including hardness, thermal shock resistance and creep resistance [5, 8]. Generally, these additives are introduced prior to sintering as transition metal carbides or as transition metal oxides if the powdered cermet is obtained through a carbothermal reduction process [9-11]. During sintering, Ti(C,N)-based cermets develop the characteristic core-rim microstructure, where the core corresponds to the original Ti(C,N) particles and the rim is the newly formed carbonitride solid solution, $(Ti,Mt_1,Mt_2\ldots)(C,N)$, which contains Ti and other

transition metal additives [12-14]. The rim phase is believed to be responsible for the good mechanical behavior of cermets [15, 16]; therefore, these carbonitride solid solution phases have been proposed for use as raw ceramic materials [17].

It has been shown that the mechanically induced self-sustaining reaction (MSR) provides access to complex carbonitride phases, which use more than one transition metal [18, 19]. This reactive milling method exploits the highly exothermic nature of the carbonitride formation reaction, which produces complex solid solutions via the combustion process and allows good stoichiometric control. It has also been shown that these complex carbonitrides may be used as a unique raw ceramic material in the development of cermets [6, 20, 21], providing greater control over the final ceramic composition and cermet microstructure.

The aim of this work was to characterize the microstructure and mechanical behavior of cermets based on titanium-tantalum carbonitrides, $Ti_xTa_{1-x}C_{0.5}N_{0.5}$, as a function of the Ta content. The powdered cermets containing $Ti_xTa_{1-x}C_{0.5}N_{0.5}$ as the ceramic phase were synthesized by MSR and subsequently densified using a pressureless process. Several microstructural parameters, including the ceramic particle size, binder phase content, porosity, ceramic contiguity and binder mean free path, were measured and correlated with the mechanical properties. The mechanical characterization included determining the Vickers and nano-indentation hardnesses, fracture toughness (conventional indentation microfracture), dynamic Young's modulus (using a non-destructive ultrasound technique) and biaxial strength (using the ball on three balls technique). A fractographic examination was also performed to estimate the size of the critical processing flaws.

2. EXPERIMENTAL

2.1. Processing of cermets.

A set of five (Ti,Ta)(C,N)-Co cermets with different nominal Ta/Ti ratios were prepared from elemental powder mixtures. Titanium powder (99% purity, < 325 mesh, Strem Chemicals), tantalum powder (99.6% purity, < 325 mesh, Alfa-Aesar), graphite powder (< 270 mesh, Fe ≤ 0.4%, Merck), cobalt powder (99.8% purity, < 100 mesh, Strem Chemicals) and nitrogen (H_2O and O_2 ≤ 3 ppm, Air Liquide) were used to synthesize the powdered cermets using MSR.

As shown in Table I, a powder mixture containing 46.5 g of elemental Ti, Ta, C and Co along with 13 tempered steel balls (d = 20 mm, m = 32.6 g) were introduced to a 300 ml tempered steel vial. The mixtures were milled using a modified planetary ball mill (Pulverisette 4, Fritsch) at a spinning rate of 400 rpm under 6 atm of nitrogen gas. The planetary mill enabled the self-propagating reactions to be monitored during the milling process by continuously measuring the pressure inside the vial [22]. When the self-propagating reaction associated with the formation of the carbonitride phase occurred, the temperature increased due to the release of heat from the exothermic reaction, which consequently increased the total pressure. The ignition time, defined as the critical milling time required to induce the MSR process, could then be determined from the spike in the recorded time–pressure data (Table I). After ignition, the milling was continued for 30 min to ensure full conversion and homogenization.

Powdered cermets obtained by MSR were molded using a uniaxial press (2 tons, 5 min) and then compacted using the cold isostatic pressing technique (200 MPa, 10 min). The green bodies were sintered between 1450 ºC and 1550 ºC for 60 min (heating

and cooling rates of 5 ºC/min) under a flow of Ar ($H_2O \leq 8$ ppm and $O_2 \leq 2$ ppm, Linde) in a horizontal tubular furnace (IGM1360 model no. RTH-180-50-1H, AGNI) to afford cylindrical cermets that were 13 mm in diameter and 9 mm in height. The sintering temperature was optimized for each Ta/Ti ratio (Table II).

2.2. Chemical, microstructural and physical characterization.

X-ray diffraction patterns of the powders and polished surfaces of the cermets were obtained using a PANalytical X'Pert Pro instrument equipped with a Θ/Θ goniometer, a Cu K_α radiation source (40 kV, 40 mA), a secondary K_β filter and an X'Celerator detector. The diffraction patterns were obtained by scanning from 20 to 140 º(2θ) in the step-scan mode with 0.02 º steps and a counting time of 275 s/step. Silicon powder (Standard Reference Material 640c, NIST) was used to calibrate the positions of the diffraction lines. The space group symmetry and the lattice parameters were calculated from the complete set of peaks in the XRD pattern using the FULLPROF Suite free software, containing the DICVOL, WinPLOTR and FullProf computer programs [23].

The scanning electron microscopy (SEM) images of the polished and fracture surfaces of the cermets were obtained using a Hitachi S- 4800 SEM-Field Emission Gun microscope. Image analysis (IA) with the Image-Pro Plus 6.2 software was employed to obtain the microstructural parameters from the SEM micrographs using the linear intercept method [24]. The main parameters determined using this method were as follows: i) the particle size of the carbonitride phase, *d*; ii) the volume fraction of the

binder phase, *FB*; iii) the contiguity of carbonitride particles, *C;* and iv) the binder mean free path, λ, which was determined from *d*, *FB* and *C* using the Roebuck equation [25].

The transition metal content in the ceramic and binder phases was measured using an energy dispersive X-ray spectrometry (EDX) detector coupled to the SEM. The overall carbon and nitrogen content in the cermets was determined by C, N elemental analysis using the LECO elemental analyzer (mod. CNHS-932).

The bulk density measurements were performed using Archimedes' distilled water impregnation method because of its experimental simplicity and reasonable reliability (ASTM C373- 88). The porosity was evaluated by image analysis (IA) using a Nikon Epiphot optical microscope (OM) coupled to a Jenoptik Progress C3 camera and Image Pro-Plus 6.2 analysis software.

2.3. Macro and micromechanical behavior.

The dynamic Young's modulus was measured using a Krautkramer USM 35 ® flaw detector from the longitudinal (V_L) and transverse (V_T) propagation velocities of acoustic waves. The wave velocity through the sample was measured by minimizing the delay time of the transducers and following an iterative measurement protocol. The dynamic Young's modulus was calculated from the density (g/cm^3), V_L and V_T. [26].

The hardness was measured at 5 kgf (HV5) using a Vickers diamond pyramidal microindenter (Zwick 3212) on the polished surfaces of the cermet. This load was chosen to avoid artifacts from the indentation load effect and to evaluate the influence of the microstructure of the material as discussed in previous studies [27]. Ten indentations were made for each specimen. The fracture toughness, K_{Ic}, was evaluated

using the indentation microfracture (IM) method using the equations from Shetty et al. [28]. This method has been proven to be applicable to a variety of relatively low-toughness cemented carbides [29]. The accurate measurement of the surface length of the arrested cracks was performed by OM and SEM.

Nano-indentation was performed using a Nano-indentation Hardness Tester TTX-NHT (CSM Instruments). The Berkovich pyramid diamond tip was used in the simple loading/unloading regime. The resulting load-penetration (P-h) curves were evaluated using the Oliver and Pharr analysis [30], from which the hardness and elastic modulus values were calculated. The response from individual phases was measured using the grid method, where 100 indentations were made with maximum load of 20 mN. The indentations were then observed using a confocal microscope (Plu Neox by Sensofar), and the measured values were attributed to the different phases (ceramic and binder).

The flexural strength was measured using the ball on three balls test (B3B-test), where a disc specimen was supported on three balls and loaded symmetrically by the fourth ball. The diameters of all four balls were 3 mm. The three-point support guarantees that there are three well-defined point contacts. In addition, a biaxial tensile stress state is observed at the midpoint of the disc's surface opposite the loading ball, which is used for the testing of biaxial strength. Additional details about this test can be found elsewhere [31]. The tensile-loaded surfaces of the B3B specimens (disks with a thickness of 1 mm and a diameter of 12 mm) were carefully ground and polished to avoid surface damage. The biaxial flexural test was performed using an electromechanical universal testing machine. A pre-load of 10 N was applied to maintain the specimen between the four balls. The tests were conducted at room

temperature under load control at a rate of 100 N/s. The load was increased until fracture, and the fracture load was used to calculate the maximum tensile biaxial stress, σ, in the specimen at the moment of fracture. Five specimens were evaluated for each sintered cermet.

The fracture strength was statistically analyzed as a function of stress, which was related to a certain failure probability, P_f, using the two-parameter Weibull distribution:

$$P_f(V_0) = 1 - \exp\left[-\left(\frac{\sigma}{\sigma_0}\right)^m\right] \quad (1)$$

where σ_0 and m are constants for the characteristic strength and Weibull modulus, respectively. The failure probability is related to the effective volume or area examined. Characteristic strength values were evaluated with a probability of failure of P_f = 63.21%. The determination of the Weibull distribution is standardized according to EN 843-5, meaning that it must be measured on "at least" 30 specimens. However, because machining costs are high, it is not common practice to test such a large number of specimens.

The Weibull modulus is generally biased by the number of specimens, *N*. The correction factor values were tabulated as a function of the number of test specimens, which can be found in the ISO 20501:2003(E). The standard deviation of the Weibull parameters (σ_0 y m) can be estimated for a fixed number of specimens using the following equations:

$$S_{\sigma_o} = \frac{\sigma_o}{m\sqrt{N}} \quad (2)$$

$$S_m = \frac{m}{\sqrt{N}} \qquad (3)$$

Select specimens were evaluated by SEM after the mechanical testing to obtain a detailed fractographic examination and discern the fracture micromechanism. A comparison of the estimated and experimentally determined critical flaw sizes was determined using the IM method and by measuring defects using fractography within the framework of linear elastic fracture mechanics (LEFM).

3. RESULTS AND DISCUSSIONS.

3.1 Chemical, microstructural and physical characterization.

The XRD patterns of the powdered cermets obtained by MSR (Figure 1a) revealed the formation of major phases with a cubic structure and *Fm-3m* space group symmetry that could be ascribed to a titanium-tantalum carbonitride solid solution. The structure was further confirmed by comparison with the reference diffraction patterns of TiN (38-1420), TiC (32-1383), TaC (35-0801), and TaN (49-1283). A gradual shift in the XRD reflections to lower 2θ values was observed when increasing concentrations of Ta were introduced to the mixture (Figure 1b) [18]. This shift provides clear evidence of the increasing Ta content in the carbonitride structure. In contrast, the C and N elemental analysis revealed that all samples exhibited the same C/N atomic ratio of 2.7 (73% C, 27% N). Because the presence of C and N can only be attributed to the carbonitride ceramic phase due to the low solubility of C and N in the cobalt binder phase [21], the C and N content was considerably different from the expected initial nominal composition. Moreover, no other carbon- and/or nitrogen-containing phases were detected by XRD and SEM.

The lattice parameter of the ceramic phase, as determined using the FullProf software, reflects the different Ta–Ti composition in the carbonitride phase (Table I). Figure 2 shows good agreement between the experimental results and the theoretical lattice parameters of a hypothetical $Ti_xTa_{1-x}C_{0.73}N_{0.27}$ solid solution that was calculated assuming the rule of mixtures, the Ta–Ti nominal compositions of Table I and the C/N ratio as determined by elemental analysis. A slight deviation from the theoretical values (dotted line in Figure 2) is attributed to the incorporation of some of the initial Ti and Ta into the binder phase during the MSR process. Moreover, a greater deviation was observed with increasing Ta content because more Ta was incorporated into the binder than Ti. As discussed later, this effect is also illustrated by the EDX analyses performed on the cermets.

Furthermore, note that the XRD patterns of the powdered cermets did not reveal the presence of Co (the presumed binder phase), which was also added to the mechanochemical reaction. Instead, a wide reflection band was observed at approximately 43 °–44 °, which could be associated with the existence of the Ti–Ta-Co alloy. This alloy was likely to form during the MSR reaction and was triggered by the heat released from the highly exothermic carbonitride formation [21]. The existence of Ti and Ta in this alloy explains why the carbonitride solid solution exhibited a higher carbon content than expected from the initial nominal composition, as well as the previously observed deviation in the lattice parameters.

The XRD patterns of the sintered cermets (Figure 3) reveal that reflections corresponding to the $Ti_xTa_{1-x}C_{0.73}N_{0.27}$ ceramic phase remained essentially at the same 2θ position as those of the powdered cermets. A small displacement was attributed to

the formation of a rim phase with a slightly higher Ti content during sintering [21]. This finding is also confirmed by the SEM characterization discussed later.

New reflections were observed in the binder phase upon sintering, which were assigned to Ti–Ta–Co intermetallic compounds [20, 21]. The sTi100 cermet exhibited a majority TiCo phase and a minority $TiCo_2$ phase with a cubic structure and *Pm-3m* and *Fd3m* space group symmetry, respectively. When the amount of Ta was increased in the initial mixture, the amount of the 1:1 intermetallic ($Ti_xTa_{1-x}Co$) decreased, whereas the amount of the 1:2 compound ($Ti_xTa_{1-x}Co_2$) increased. Both intermetallics were also observed in sTi99Ta01 and sTi95Ta05 cermets, but only the cubic $Ti_xTa_{1-x}Co_2$ intermetallic compound was found in the sTi90Ta10 and sTi80Ta20 cermets. This trend can be explained by the inability of Ta to replace the high proportion of Ti in the TiCo cubic structure. According to the Ti-Co and Ta-Co phase diagrams, a TaCo compound with a 1:1 stoichiometry and with the same structure as that of TiCo does not exist. However, $TaCo_2$ and $TiCo_2$ intermetallics with the same structure and space group symmetry exist, making it possible to observe the $(Ti_xTa_{1-x})Co_2$ solid solution.

The microstructure of the cermets was characterized by SEM, and representative micrographs are presented in Figure 4. Cermets with higher Ta content exhibited the characteristic core–rim microstructure, but with an inverse contrast compared with the one typically observed in the literature (wherein the rim exhibits a darker contrast than the core). As expected, the core–rim microstructure was not observed in cermets without Ta, but it also could not be observed in cermets with a low Ta content due to negligible contrast differences in the SEM images. Both the core and the rim were composed of $Ti_xTa_{1-x}C_{0.73}N_{0.27}$ solid solutions, but the rim simply exhibited a higher Ti content. This finding was confirmed by the semi-quantitative EDX-SEM analyses, as

indicated by the solid arrows in Figure 4. This inverse core–rim microstructure has already been reported [21], and it was caused by the well-known phenomenon of dissolution-reprecipitation of carbonitrides particles during sintering. The combined effect of using the $Ti_xTa_{1-x}C_{0.73}N_{0.27}$ solid solution and not a mixture of TiC_xN_{1-x} and TaC as the ceramic raw material, as well as the presence of Ti and Ta in the binder, produced this unusual microstructure.

Similarly, the binder phase's composition was also determined using EDX-SEM, and the characteristic values are indicated in Figure 4 by the dotted arrows. The compositions are in agreement with the XRD results, which confirmed the presence of Ti and Ta in the binder. Two binder phases with different composition were observed in sTi100, sTi99Ta01 and sTi95Ta05, corresponding to $(Ti_xTa_{1-x})Co_2$ and $(Ti_xTa_{1-x})Co$. In sTi90Ta10 and sTi80Ta20, only $(Ti_xTa_{1-x})Co_2$ was found. These phases are in accordance with the reference diffraction patterns of $TiCo_2$ (17-0031), $TaCo_2$ (15-0030) and TiCo (18-0429). Moreover, the EDX analyses also revealed that a greater amount of Ta was incorporated into the binder, which supported the fact that the Ta content in the carbonitride phase was lower than expected from the nominal initial stoichiometry.

The ceramic particle size distribution determined from the SEM images confirmed the trend observed in Figure 4, which showed a significant reduction in the average ceramic particle size, d_{av}, as well as a narrowing of the size distribution with increasing tantalum content in the cermets (Figure 5 and Table II). To make this effect more visible, $d_{50\%}$ and $d_{90\%}$ values corresponding to 50 and 90 percentiles are also included in Figure 5. These results suggest that the phenomena of dissolution-reprecipitation of the $Ti_xTa_{1-x}C_{0.73}N_{0.27}$ solid solution particles were hindered by the presence of Ta. Likewise, the volume content of the binder phase, *FB*, was also

measured by image analysis, and two trends were observed with increasing Ta content (Figure 6a and Table II). The high content observed in sTi100 was attributed to the presence of a majority phase composed of a TiCo intermetallic with 1:1 stoichiometry. When Ta was introduced to the system, the nature of the binder became more intermetallic at the 1:2 stoichiometry ($Ti_xTa_{1-x}Co_2$) with a corresponding reduction in the *FB*. In the case of the sTi95Ta05 cermet, practically only the $Ti_xTa_{1-x}Co_2$ intermetallic compound was observed, and the *FB* increased again due to the greater substitution of Ti by Ta in the $Ti_xTa_{1-x}Co_2$ structure.

Figure 6b and Table II show the evolution of two important microstructural parameters, *C* and λ, as a function of the initial nominal Ta content. The highest λ value was observed for the sTi100 cermet, which also exhibited the highest *FB* and *d* values. For the rest of the cermets, λ decreased gradually with the increasing incorporation of Ta. In contrast, a *C* value of approximately 0.4 was observed for all cermets, and the small variations appeared to follow an inverse behavior as that of *FB*.

Density measurements of the sintered cermets were performed using the Archimedes method, and the expected increase in the density with increasing Ta content was observed (Table II). To assess the quality of the sintering process, the porosity of the cermets was also determined by image analysis (Table II). Samples sTi100, sTi99Ta01, and sTi95Ta05 exhibited porosity values of less than 1%; the porosity increased in cermets with a higher Ta content, reaching approximately 3% in sTi80Ta20. This trend was in agreement with the observed difficulties in properly sintering the cermets containing higher Ta content, which required the use of higher temperatures because of the presence of higher melting Ta in the binder. Although the porosity level

was low, it had to be taken into account because of its effect on the mechanical properties, especially the flexural biaxial strength.

3.2 Mechanical characterization.

The mechanical behavior results for the cermets are summarized in Table III. The dynamic Young's modulus, E_d, (Figure 7a and Table III), increased with increasing Ta content and the corresponding increase in density, inherent to Ta and the manufacturing process. An important initial increase was observed in samples with a lower Ta content. The behavior then became asymptotic, reaching similar E_d values for cermets with higher Ta content. Note that the Ta is present in both the ceramic and the binder phases. Taking into account the Young's modulus of TiC and TaC (400 and 560 GPa, respectively), it is expected that the Young's modulus of the $Ti_xTa_{1-x}C_{0.73}N_{0.27}$ solid solution should increase with increasing Ta content. Similarly, considering the Young's modulus of Co, Ta and Ti (209, 186 and 116 GPa, respectively), it is also expected that intermetallic compounds of the binder phase with higher Ta content should exhibit higher E_d values.

The high Young's modulus of the cermets, which was on the same order of magnitude as that of the ceramic phase, can be related to the low metallic character of intermetallic compounds with properties closer to those of ceramics [32, 33]. Nanoindentation tests performed on sTi95Ta05 and sTi90Ta10 cermets make it possible to study the response of the individual ceramic and the binder phases (Figure 8). The results shown in Table IV confirmed that the binder phase exhibited a hardness and Young's modulus similar to those of the carbonitride phase and quite different from that of Co (HV= 1.04 GPa; E=209 GPa).

Figure 7b and 7c show the evolution of HV5 and K_{Ic} with increasing Ta content and λ, respectively. The Vickers hardness value remained unchanged within the error of the measurement (Table III). However, after reaching a maximum HV5 value for cermet sTi95Ta05, HV5 began to decrease with increasing Ta content, which could be a result of variation in the *FB*. A comparison of Figures 6a and 7b reveals that the maximum hardness corresponds to the cermet with the lowest *FB* value.

Furthermore, a direct relationship was observed between K_{Ic} and λ, which was inverse of the Ta content (see Figures 7b and 7c). The increase in the binder constriction of cermets with a high Ta content (smaller carbonitride particle size) limited the effectiveness of the ligaments (capability to absorb plastic energy during the fracture process). Within this framework, another important toughening mechanism involving the phenomenon of crack deflection is also directly related to d and λ. In contrast, the low observed values were attributed to the presence of brittle intermetallic compounds in place of metal in the binder.

The biaxial flexural strength behavior was evaluated, and the results are shown in Table III, where the absolute values and confidence intervals associated using the conventional protocol (probability of failure of 50%) and the Weibull analysis (σ_0 and m; probability of failure of 63.21%) are presented. The standard deviation of the Weibull parameters was determined for a fixed number of specimens (5 in this case). Figure 7d shows the Weibull-distributed data in terms of the probability of failure vs. the fracture strength as a straight line after rearranging and taking double logarithm in equation 1. The results indicate that the cermets with lower (sTi100, sTi99Ta01 and sTi95Ta05) and higher (sTi90Ta10 and sTi80Ta20) Ta contents exhibit a statistically significant difference in the equivalent characteristic strength. The maximum

mechanical strength was reduced drastically in specimens sTi90Ta10 and sTi80Ta20, which exhibited high Ta content, as a result of higher porosity and sintering difficulties due to the increasing Ta content.

No statistically significant differences were found in the Weibull moduli (mechanical reliability), suggesting similar flaw populations. The only exception was for cermet sTi99Ta01, which exhibited a considerably higher Weibull modulus and characteristic strength (20 and 572 MPa, respectively). For this cermet, the specimens broke in a narrow range of stresses, which indicates higher mechanical reliability in terms of design. The maximum resistance could be related to the minimum value of contiguity obtained suggesting the presence of a lower number of binderless carbonitride clusters, which are typical defects at the origin of fractures.

The analysis of fracture surfaces (Figure 9) revealed transgranular cleavage breaking up the carbonitride particles, which is the typical micromechanism of materials with brittle behavior. In addition, the fracture surface observations confirmed previous conclusions about the effect of porosity and ceramic particle size. Higher porosity and smaller ceramic particles were observed in cermets with higher Ta content, sTi90Ta10 and sTi80Ta20. A more detailed analysis using a higher magnification (Figure 10) revealed the presence of river patterns within the grains, i.e., multiple lines that converge into one, as a result of a cleavage following the second order planes. In addition, tongues, or small elevations on cleavage planes, were associated with the presence of micro twins. Moreover, the critical flaw sizes were experimentally measured by performing a fractographic examination, and the results are provided in Table V. These experimental values are in good agreement with those estimated by

combining the results from the fracture toughness evaluation and biaxial strength measurements (Weibull analysis) [flaw sizes and geometry factor $Y=2/\pi$)].

CONCLUSIONS

The MSR process was used to develop cermets based on complex tantalum and titanium carbonitride ($Ti_xTa_{1-x}C_{0.73}N_{0.27}$) phases with various transition metal compositions. By increasing the Ta content in the carbonitride solid solution, the size of the ceramic particles was reduced, resulting in cermets with an inverse core-rim microstructure.

The evolution of the mechanical properties of the cermets, such as the E_d, HV5 and K_{Ic}, was correlated not only with the Ta content but also with the microstructural parameters. A direct relationship was observed between the E_d, Ta content and density. The hardness values did not appear to vary with Ta content, as was observed with the *FB* values. At the same time, the Ta content exhibited an important effect on the toughness (K_{Ic}), wherein the value decreased with increasing Ta concentration, revealing a direct relationship between K_{Ic} and λ. This effect was mainly due to a reduction in the ceramic particle size at higher Ta contents. Furthermore, the low K_{Ic} values observed for all cermets were attributed to the presence of intermetallic compounds in the binder phase, which caused the developed materials to behave more like a ceramic-intermetallic composite than a cermet.

The biaxial flexural strength behavior revealed that the maximum mechanical strength was reduced significantly in specimens with a high Ta content. This effect was related to higher porosity content due to the difficulty encountered with properly sintering cermets with high Ta content. The Weibull modulus and characteristic strength

for the sTi99Ta1 were considerably higher (20 and 572 MPa, respectively), suggesting a higher mechanical reliability. The maximum resistance observed was related to the minimum value of contiguity of the carbonitride particles.

Acknowledgments

This work was supported by the Spanish government under grant No. MAT2011-22981, which was financed in part by the European Regional Development Fund of 2007-2013. E. Chicardi and J. M. Córdoba were supported by the CSIC through JAE-Pre and JAE-Doc grants, respectively, which are financed in part by the European Social Fund (ESF). The authors want to thank the laboratory technician J. Pinto and the undergraduate student D. Moreno for their assistance with mechanical testing.

REFERENCES

[1] Pastor H. Titanium-carbonitride-based hard alloys for cutting tools. Materials Science and Engineering. 1988;105-106(PART 2):401-9.
[2] Gong X, Sun J, Quan K, Meng Y. Synthesis and application of titanium carbonitride. Kunming2013. p. 2373-7.
[3] Zhang S. Titanium carbonitride-based cermets: processes and properties. Materials Science and Engineering A. 1993;163(1):141-8.
[4] Clark EB, Roebuck B. Extending the application areas for titanium carbonitride cermets. International Journal of Refractory Metals and Hard Materials. 1992;11(1):23-33.
[5] Ettmayer P, Kolaska H, Lengauer W, Dreyer K. Ti(C,N) Cermets - Metallurgy and Properties. International Journal of Refractory Metals and Hard Materials. 1995;13(6):343.
[6] Córdoba JM, Alcalá MD, Avilés MA, Sayagués MJ, Gotor FJ. New production of TiCxN1-x-based cermets by one step mechanically induced self-sustaining reaction: Powder synthesis and pressureless sintering. Journal of the European Ceramic Society. 2008;28(10):2085-98.
[7] Manoj Kumar BV, Kumar JR, Basu B. Crater wear mechanisms of TiCN-Ni-WC cermets during dry machining. International Journal of Refractory Metals and Hard Materials. 2007;25(5-6):392-9.
[8] Alvarez M, Sánchez JM. Spark plasma sintering of Ti(C, N) cermets with intermetallic binder phases. International Journal of Refractory Metals and Hard Materials. 2007;25(1):107-18.
[9] Zhang S, Khor KA, Lü L. Preparation of Ti(C,N)-WC-TaC solid solution by mechanical alloying technique. Journal of Materials Processing Tech. 1995;48(1-4):779-84.
[10] Monteverde F, Medri V, Bellosi A. Synthesis of ultrafine titanium carbonitride powders. Applied Organometallic Chemistry. 2001;15(5):421-9.

[11] Jin Y, Liu Y, Wang Y, Ye J. Synthesis of ultrafine (Ti, W, Mo, V)(C, N)-Ni composite powders by low-energy milling and subsequent carbothermal reduction-nitridation reaction. Journal of Alloys and Compounds. 2009;486(1-2):L34-L6.
[12] Ahn SY, Kang S. Formation of core/rim structures in Ti(C,N)-WC-Ni cermets via a dissolution and precipitation process. Journal of the American Ceramic Society. 2000;83(6):1489-94.
[13] Guo Z, Xiong J, Yang M, Wang J, Sun L, Wu Y, et al. Microstructure and properties of Ti(C,N)-Mo 2C-Fe cermets. International Journal of Refractory Metals and Hard Materials. 2009;27(4):781-3.
[14] Mari D, Bolognini S, Feusier G, Cutard T, Viatte T, Benoit W. TiMoCN based cermets Part II. Microstructure and room temperature mechanical properties. International Journal of Refractory Metals and Hard Materials. 2003;21(1–2):47-53.
[15] Isobe, Kitagawa, Nobuyuk, Yamazaki, Isao. Titanium-based alloy. United States Patent 1999
[16] Kim S, Min KH, Kang S. Rim Structure in Ti(C0.7N0.3)-WC-Ni Cermets. Journal of the American Ceramic Society. 2003;86(10):1761-6.
[17] Kim JW, Ahn SY, Kang S. Effect of the complete solid-solution phase on the microstructure of Ti(CN)-based cermet. Int J Refract Met Hard Mat. 2009;27(2):224-8.
[18] Córdoba JM, Avilés MA, Sayagués MJ, Alcalá MD, Gotor FJ. Synthesis of complex carbonitride powders TiyMT1-yCxN1-x (MT: Zr, V, Ta, Hf) via a mechanically induced self-sustaining reaction. Journal of Alloys and Compounds. 2009;482(1-2):349-55.
[19] Córdoba JM, Sayagués MJ, Alcalá MD, Gotor FJ. Monophasic TiyNb1 - YCxN1 - x nanopowders obtained at room temperature by MSR. Journal of Materials Chemistry. 2007;17(7):650-3.
[20] Chicardi E, Córdoba JM, Sayagués MJ, Gotor FJ. Absence of the core-rim microstructure in Ti xTa 1 - XC yN 1 - y-based cermets developed from a pre-sintered carbonitride master alloy. International Journal of Refractory Metals and Hard Materials. 2012;33:38-43.
[21] Chicardi E, Córdoba JM, Sayagués MJ, Gotor FJ. Inverse core-rim microstructure in (Ti,Ta)(C,N)-based cermets developed by a mechanically induced self-sustaining reaction. International Journal of Refractory Metals and Hard Materials. 2012;31:39-46.
[22] Suryanarayana C. Mechanical alloying and milling. Progress in Materials Science. 2001;46(1-2):1-184.
[23] Rodriguez-Carvajal J. FULLPROF software. 2010.
[24] Thorvaldsen A. The intercept method .2. Determination of spatial grain size. Acta Materialia. 1997;45(2):595-600.
[25] Roebuck B, Almond EA. Deformation and fracture processes and the physical metallurgy of WC-Co hardmetals. . International Materials Reviews. 1988;33(2):90-110.
[26] Nondestructive evaluation and quality control. Metals Handbook. Ninth Edition. 1989;235.
[27] Chicardi E, Torres Y, Córdoba JM, Sayagués MJ, Rodríguez JA, Gotor FJ. Effect of sintering time on the microstructure and mechanical properties of (Ti,Ta)(C,N)-based cermets. International Journal of Refractory Metals and Hard Materials. 2013.
[28] Shetty DK, Wright IG, Mincer PN, Clauer AH. Indentation fracture of WC-Co cermets. Journal of Materials Science. 1985;20(5):1873-82.
[29] Niihara K, Morena R, Hasselman DPH. Indentation fracture toughness of brittle materials for palmqvist crakcs. In: Bradt Richard C, Evans AG, Hasselman DPH, Lange FF, editors. Universal Park, PA, USA: Plenum Press; 1983. p. 97-105.
[30] Oliver WC, Pharr GM. An improved technique for determining hardness and elastic-modulus using load and displacement sensing indentation experiments. J Mater Res. 1992;7(6):1564-83.
[31] Börger A, Supancic P, Danzer R. The ball on three balls test for strength testing of brittle discs: Part II: Analysis of possible errors in the strength determination. Journal of the European Ceramic Society. 2004;24(10-11):2917-28.

[32] Baker I, Munroe PR. Improving intermetallic ductility and toughness. Journal of Metals. 1988;40(2):28-31.
[33] Russell AM. Ductility in Intermetallic Compounds. Advanced Engineering Materials. 2003;5(9):629-39.

FIGURE CAPTIONS.

Figure 1. (a) X-ray powder diffraction patterns of the powdered cermets obtained by MSR as a function of the nominal composition in Table I. (●) $Ti_xTa_{1-x}C_{0.73}N_{0.27}$, *Fm3m*; and (◪) Amorphous Ti-Ta-Co alloys. (b) Magnification of XRD patterns in the 2θ range of 34º–38º showing a shift in the (111) reflection of the carbonitride phase with increasing Ta content.

Figure 2. Correlation between the experimental lattice parameter (ELP) of the ceramic carbonitride phase in powdered cermets and the theoretical lattice parameter (TLP), assuming the Ti and Ta initial nominal compositions in Table I.

Figure 3. X-ray powder diffraction patterns of cermets after sintering the synthesized powdered cermets. (●) $Ti_xTa_{1-x}C_{0.73}N_{0.27}$, *Fm3m*; (■) $(Ti_xTa_{1-x})Co_2$, *Fd3m*; and (♦) $(Ti_xTa_{1-x})Co$, *Pm-3m*.

Figure 4. SEM micrographs of sintered cermets: (a) sTi100; (b) sTi99Ta01; (c) sTi95Ta05; (d) sTi90Ta10; and (e) sTi80Ta20. The Ti, Ta and Co compositions in the ceramic (solid arrows) and binder (dotted arrows) phases as determined by EDX-SEM are shown.

Figure 5. Ceramic particle size distribution and average size of sintered cermets determined by image analysis using the linear intercept method: (a) sTi100; (b) sTi99Ta01; (c) sTi95Ta05; (d) sTi90Ta10; and (e) sTi80Ta20.

Figure 6. Microstructural parameters of sintered cermets plotted as a function of the initial Ta weight percentage: average ceramic particle size (d); volume fraction of binder phase (FB); contiguity (C); and binder mean free path (λ).

Figure 7. Mechanical properties of sintered cermets: (a) dynamic Young's modulus (E_d) and bulk density (ρ) plotted as a function of Ta weight percentage. Hardness and toughness plotted as a function of:(b) Ta weight percentage and (c) binder mean free path (λ). (d) Weibull diagram: probability of failure as a function of fracture strength obtained using B3B flexure tests.

Figure 8. (a) Representative SEM micrographs of cermets revealing the nanoindentation marks at 20 mN, which make it possible to differentiate between the ceramic and binder phases. (b) Typical indentation curves (load vs. penetration) for the ceramic and binder phases in cermets.

Figure 9. Low-magnification SEM micrographs of fractured surfaces of sintered cermets generated during biaxial flexural strength tests (ball on three balls): (a) sTi100; (b) sTi99Ta01; (c) sTi95Ta05; (d) sTi90Ta10; and (e) sTi80Ta20.

Figure 10. High-magnification SEM micrographs of fractured surfaces of sintered cermets revealing the presence of different flaws (transgranular cleavage that may cause chaotic fracture, including river patterns and a tongue, marked with straight and dotted arrows, respectively: (a) sTi100; (b) sTi99Ta01; (c) sTi95Ta05; (d) sTi90Ta10; and (e) sTi80Ta20.

Table I. Initial nominal compositions of powdered cermets synthesized by MRS, as well as the ignition time observed during milling and the experimental lattice parameter of the carbonitride phase.

Sample	Nominal Composition	Ignition time (min)	Lattice parameter, *a* (Å)
pTi100	**$TiC_{0.5}N_{0.5}$ + 20%wt.Co**	**43**	**4.306**
pTi99Ta01	**$Ti_{0.99}Ta_{0.01}C_{0.5}N_{0.5}$ + 20%wt.Co**	**43**	**4.308**
pTi95Ta05	**$Ti_{0.95}Ta_{0.05}C_{0.5}N_{0.5}$ + 20%wt.Co**	**45**	**4.314**
pTi90Ta10	**$Ti_{0.90}Ta_{0.10}C_{0.5}N_{0.5}$ + 20%wt.Co**	**40**	**4.320**
pTi80Ta20	**$Ti_{0.80}Ta_{0.20}C_{0.5}N_{0.5}$ + 20%wt.Co**	**42**	**4.333**

Table II. Sintering temperature (T_S), density (ρ), and porosity (e) as well as the microstructural parameters of cermets (ceramic particle size (d), binder volume fraction (FB), contiguity (C) and Binder mean free path (λ)).

Specimen	T_S (ºC)	ρ (g/cm^3)	e (%)	d_{av} (μm)	FB (%)	C	λ (μ)
sTi100	**1450**	**5.40**	**<1**	**4.38**	**45.4**	**0.39**	**6.62**
sTi99Ta01	**1455**	**5.44**	**<1**	**4.14**	**34.3**	**0.37**	**3.56**
sTi95Ta05	**1475**	**5.86**	**<1**	**3.48**	**30.2**	**0.46**	**2.97**
sTi90Ta10	**1500**	**6.29**	**1.3**	**2.62**	**34.9**	**0.45**	**2.80**
sTi80Ta20	**1550**	**7.17**	**3.3**	**1.73**	**38.5**	**0.42**	**1.92**

Table III. Mechanical behavior of cermets: Dynamic modulus of elasticity (E_d), Vickers Hardness measured at 5 kgf (HV5), fracture toughness (K_{Ic}) and biaxial flexural strength using the conventional protocol (probability of failure of 50%) and the Weibull analysis (σ_0 and m; probability of failure of 63.21%).

Specimen	E_d (GPa)	HV5 kgf (GPa)	K_{Ic} (MPam$^{1/2}$)	Mechanical strength (MPa)		
				Biaxial (Ball on three balls)		
				Conventional (50 %)	Statistic fracture (63 %)	
					σ_0	m
sTi100	266	11.7 ± 0.3	5.4 ± 0.2	468 ± 66	496 ± 28	8 ± 4
sTi99Ta01	317	12.0 ± 0.3	4.8 ± 0.2	557 ± 33	572 ± 13	20 ± 9
sTi95Ta05	425	12.3 ± 0.5	4.7 ± 0.2	489 ± 68	517 ± 29	8 ± 4
sTi90Ta10	475	12.2 ± 0.4	4.4 ± 0.2	278 ± 67	305 ± 30	5 ± 2
sTi80Ta20	498	11.9 ± 0.4	4.0 ± 0.1	277 ± 40	294 ± 17	8 ± 3

Table IV. Nano-hardness (H) and Modulus of Elasticity (E) values obtained at 20 mN for ceramic and binder phases.

Specimen	Carbonitride phase		Binder phase	
	H (GPa)	E (GPa)	H (GPa)	E (GPa)
sTi95Ta05	27.4 ± 0.4	430 ± 10	15.5 ± 2.0	350 ± 15
sTi90Ta10	28.6 ± 3.1	416 ± 6	18.7 ± 1.8	405 ± 20

Table V. Critical flaw sizes of 2a (μm) corresponding to sintered cermets.

Specimen	Estimated (I)	Experimental (II)	Deviation (%)
sTi100	**155**	**163**	**5**
sTi99Ta01	**107**	**116**	**8**
sTi95Ta05	**119**	**122**	**3**
sTi90Ta10	**261**	**265**	**1**
sTi80Ta20	**269**	**235**	**15**
(I) $Y = 2/\pi$; (II) SEM			

Figure 1

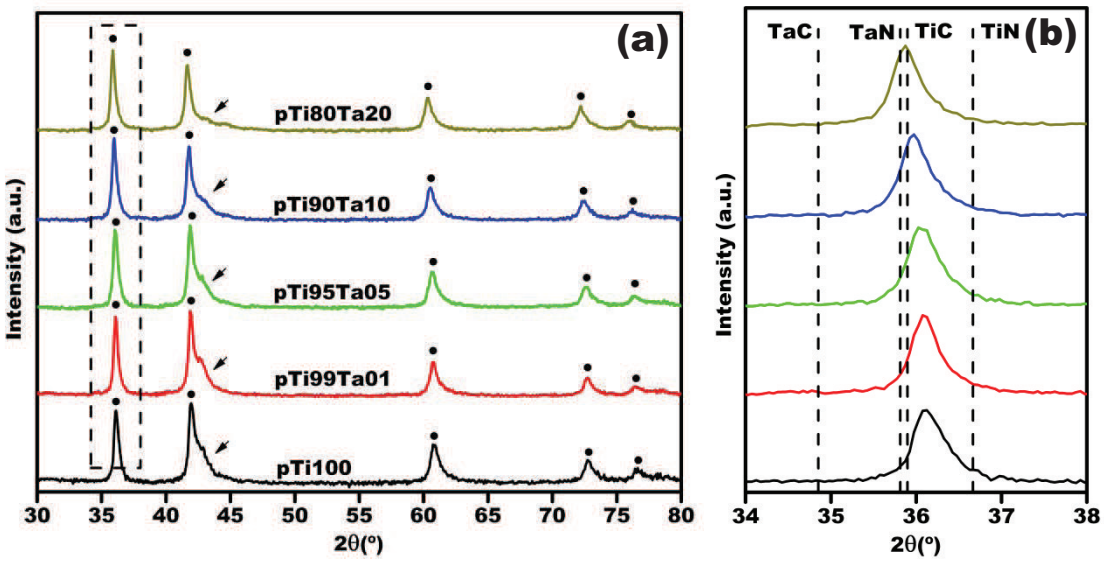

Figure 1

Figure 2

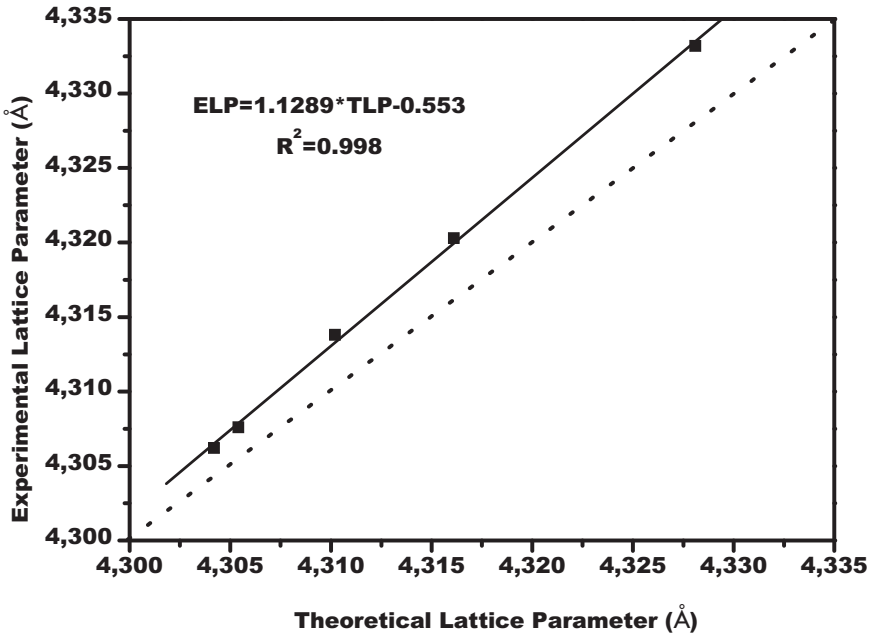

Figure 2

Figure 3

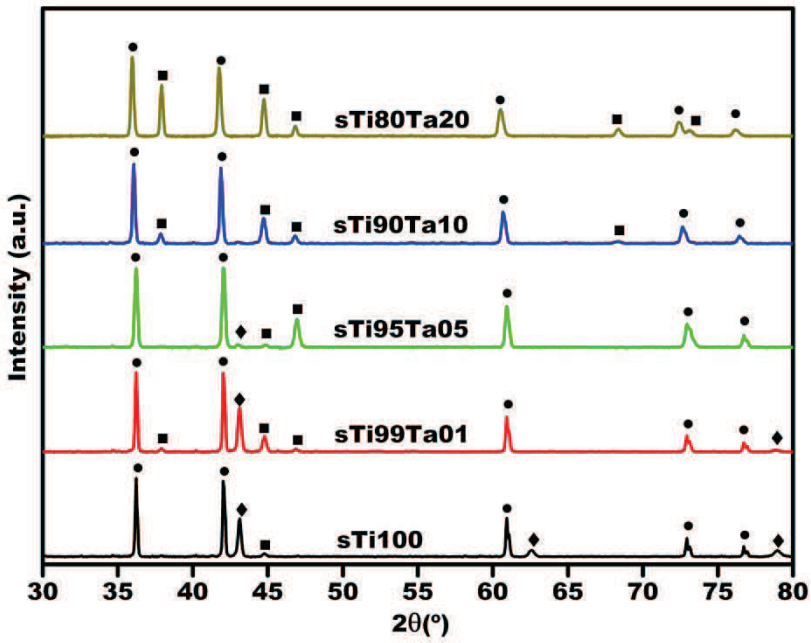

Figure 3

Figure 4

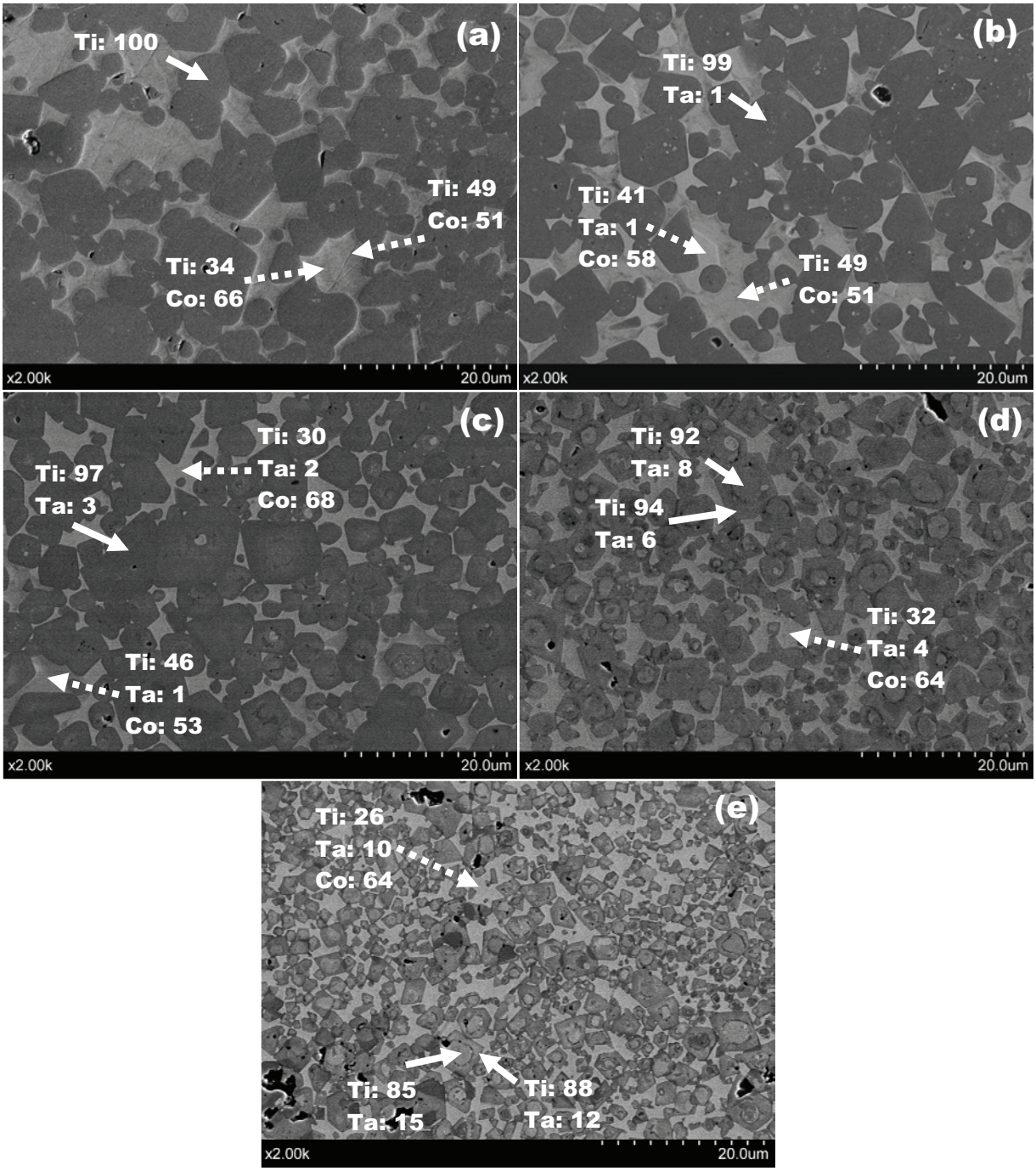

Figure 4

Figure 5

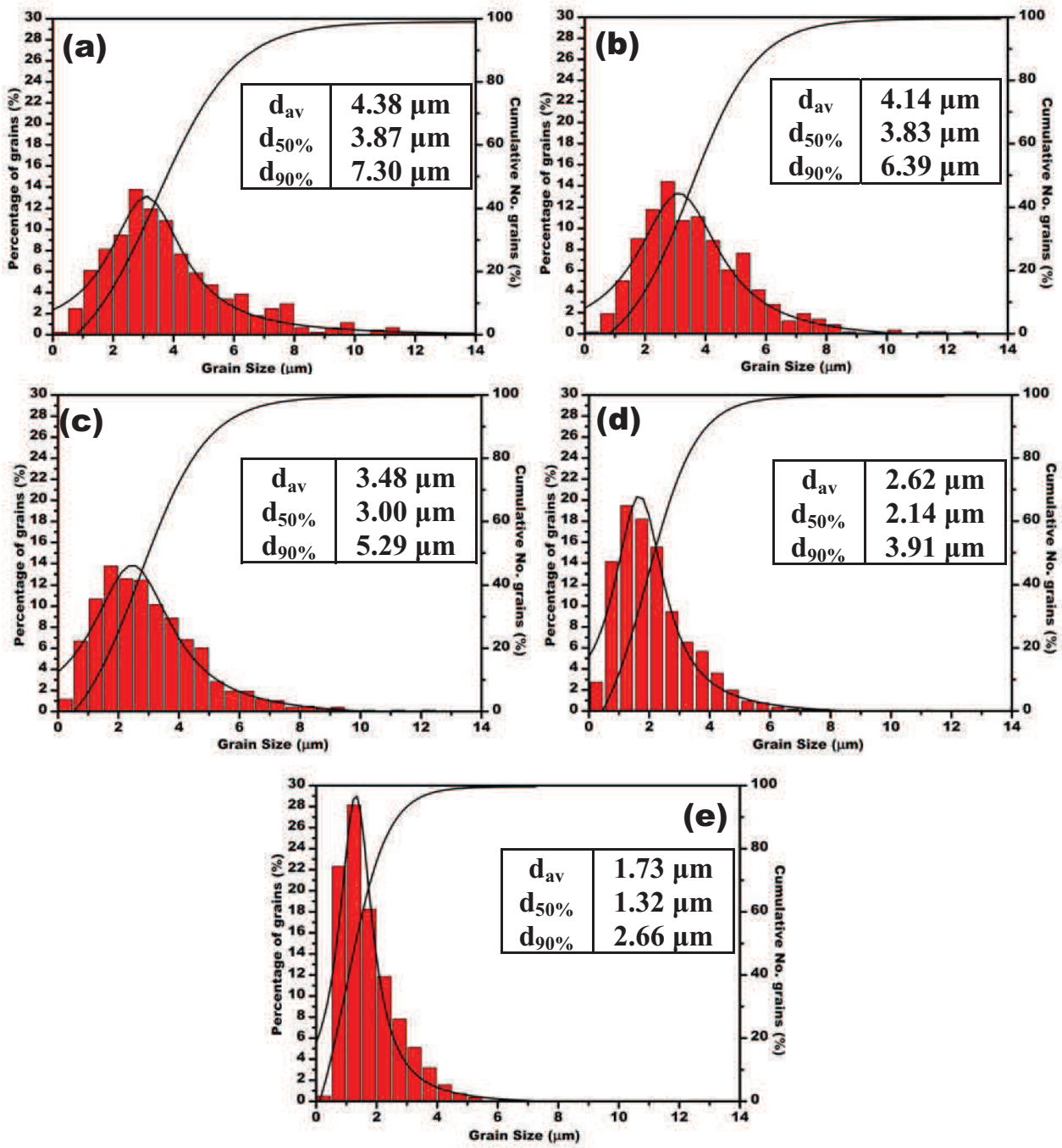

Figure 5

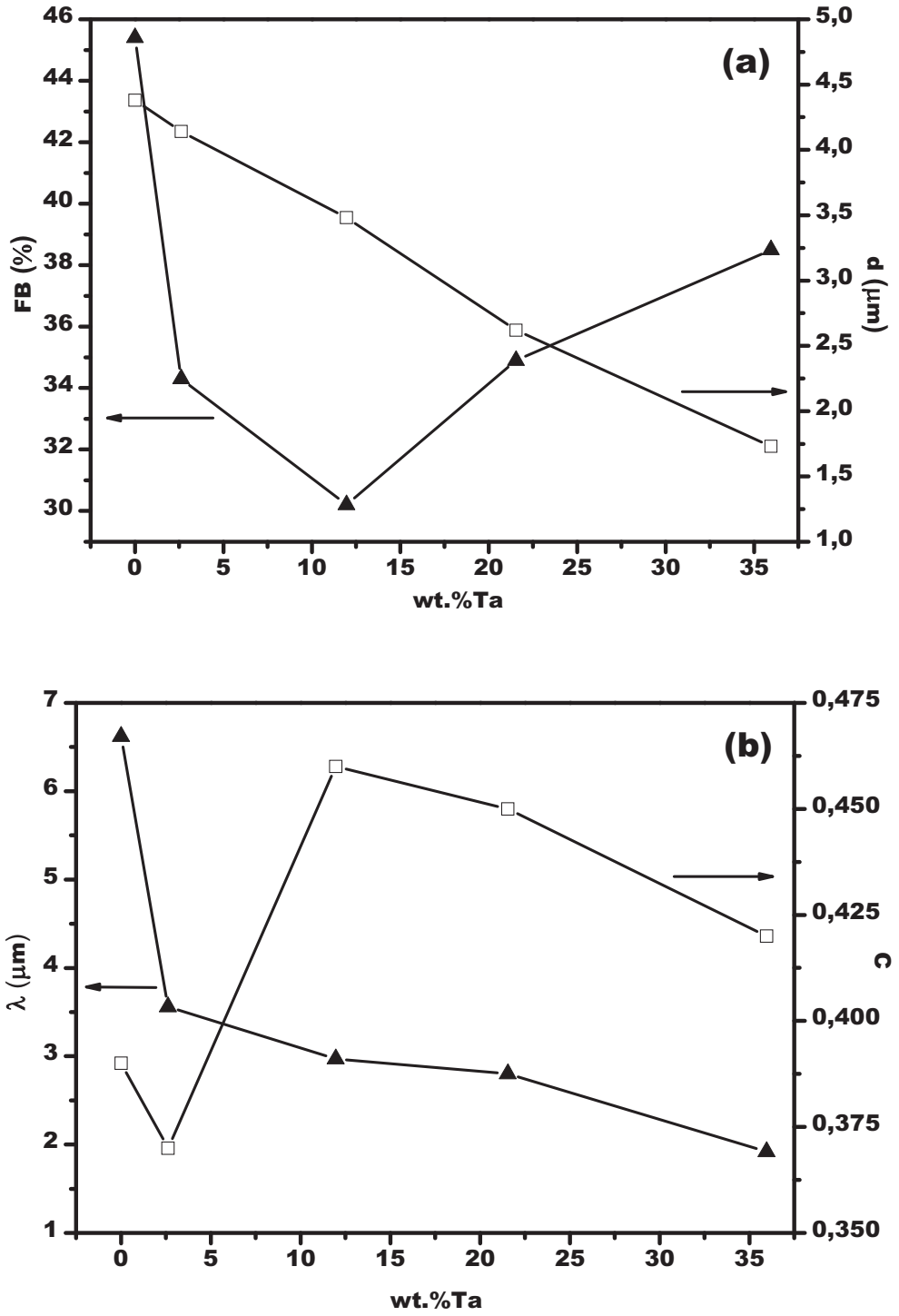

Figure 6

Figure 7

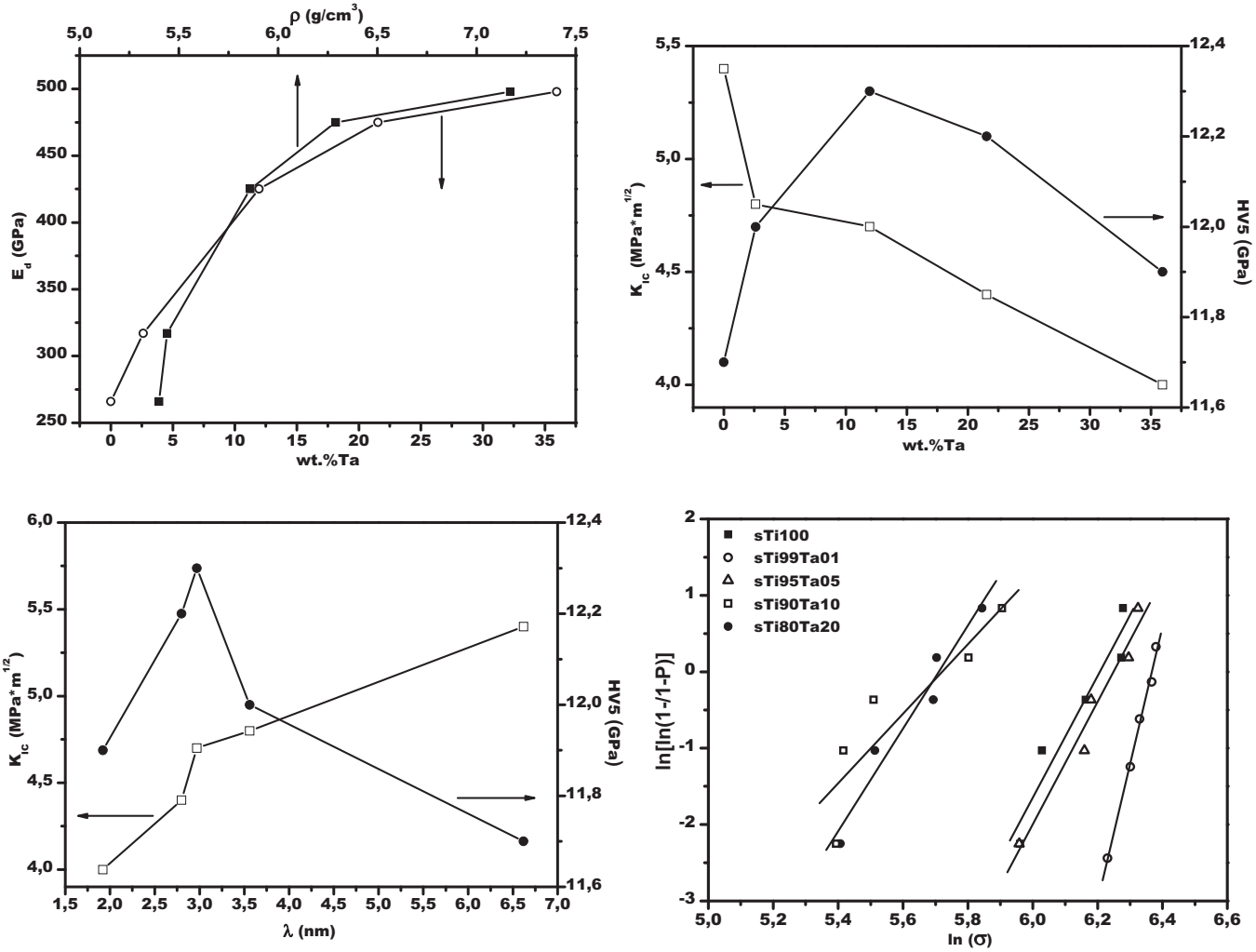

Figure 7

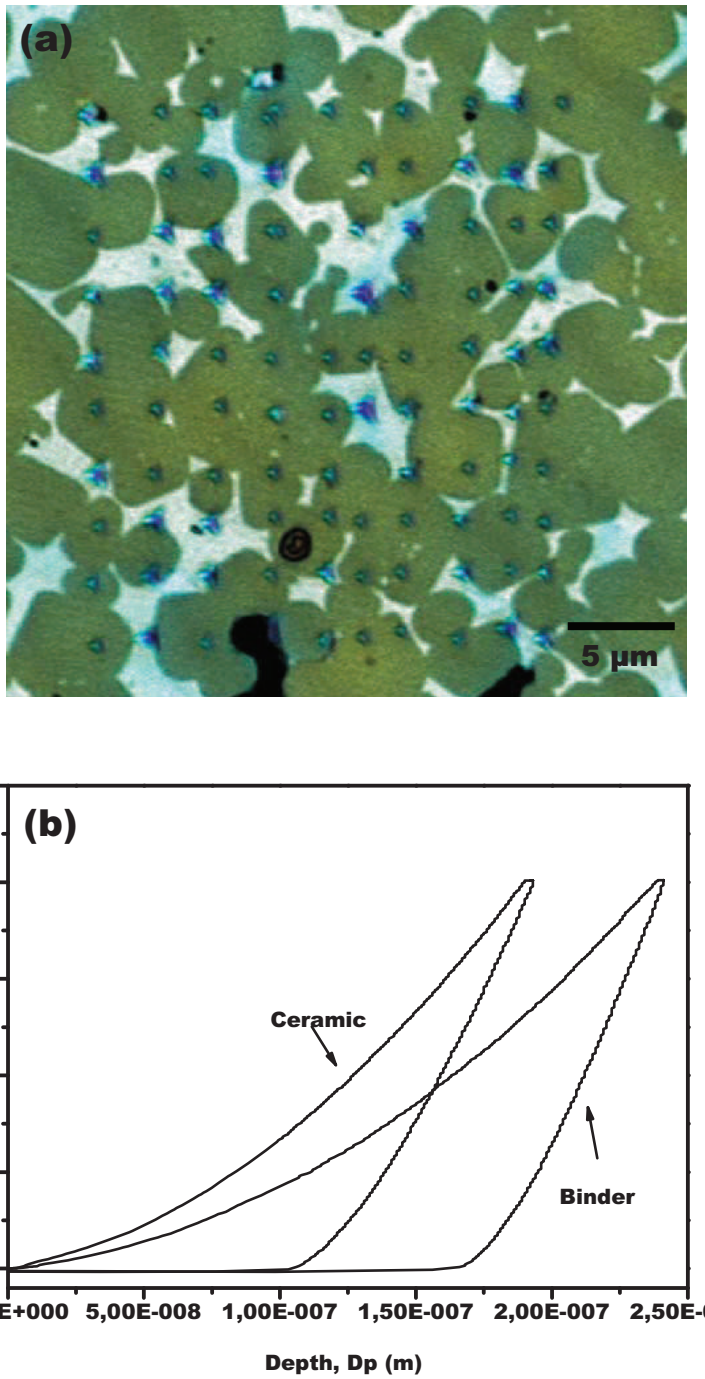
(a)
5 µm
(b)
0,025
0,020
0,015
0,010
0,005
0,000
Load, F (N)
Ceramic
Binder
0,00E+000
5,00E-008
1,00E-007
1,50E-007
2,00E-007
2,50E-007
Depth, Dp (m)

Figure 8

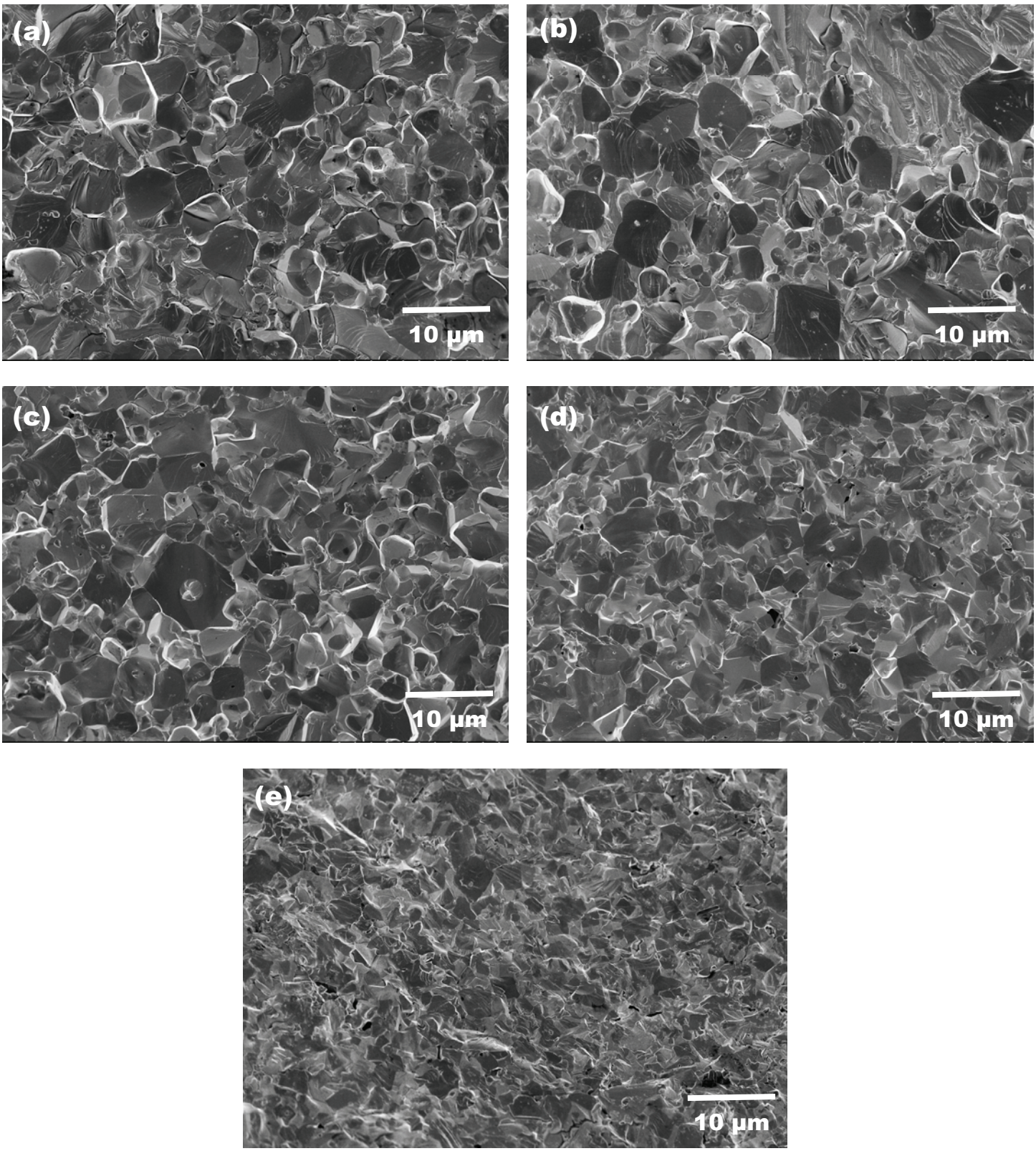

Figure 9

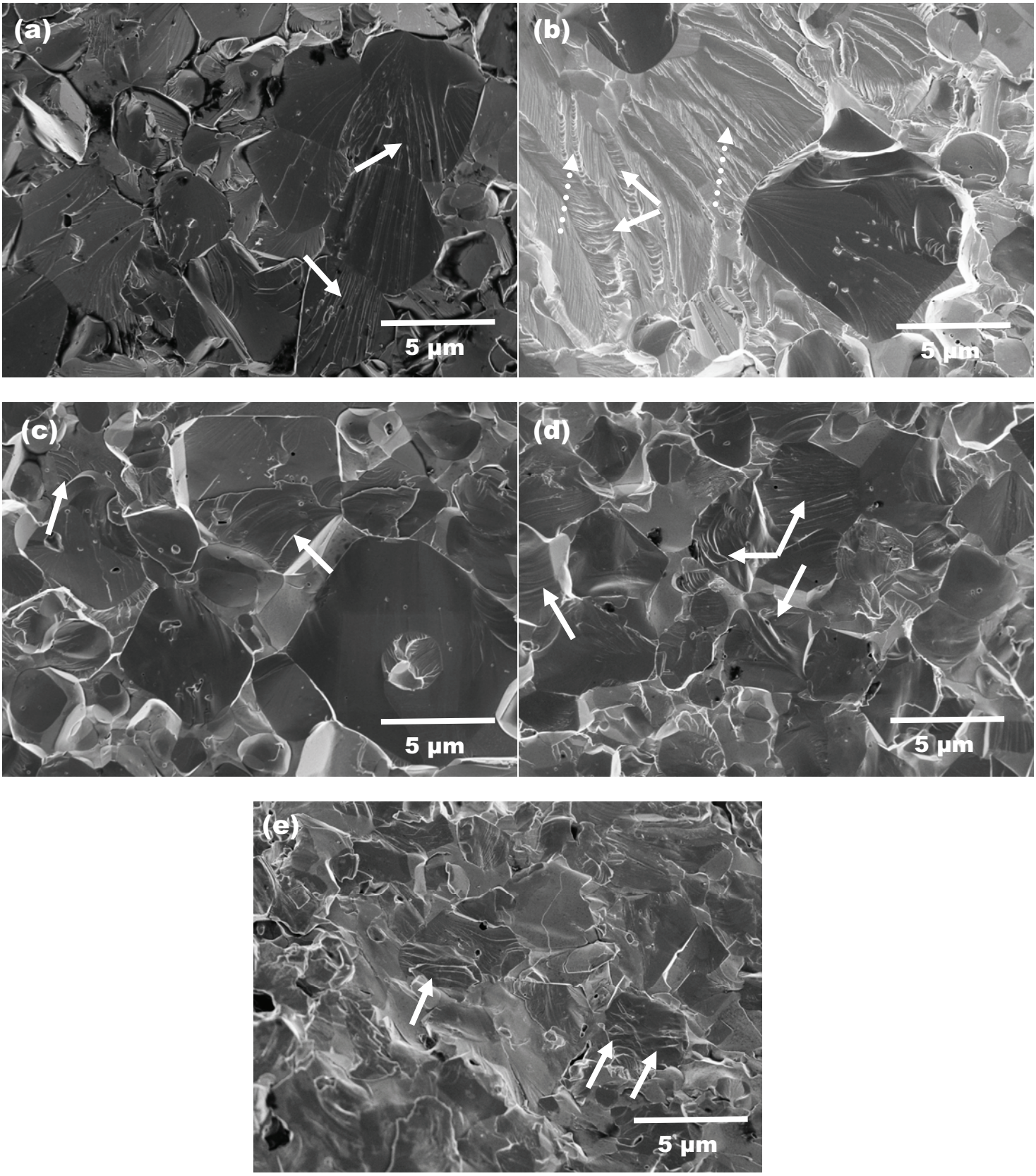

Figure 10